



Extreme thermal anisotropy in high-aspect-ratio titanium nitride nanostructures for efficient photothermal heating

Ishii, Satoshi; Higashino, Makoto; Goya, Shinya; Shkondin, Evgeniy; Tanaka, Katsuhisa; Nagao, Tadaaki; Takayama, Osamu; Murai, Shunsuke

Published in:
Nanophotonics

Link to article, DOI:
[10.1515/nanoph-2020-0569](https://doi.org/10.1515/nanoph-2020-0569)

Publication date:
2021

Document Version
Publisher's PDF, also known as Version of record

[Link back to DTU Orbit](#)

Citation (APA):
Ishii, S., Higashino, M., Goya, S., Shkondin, E., Tanaka, K., Nagao, T., Takayama, O., & Murai, S. (2021). Extreme thermal anisotropy in high-aspect-ratio titanium nitride nanostructures for efficient photothermal heating. *Nanophotonics*, 10(5), 1487-1494. <https://doi.org/10.1515/nanoph-2020-0569>

General rights

Copyright and moral rights for the publications made accessible in the public portal are retained by the authors and/or other copyright owners and it is a condition of accessing publications that users recognise and abide by the legal requirements associated with these rights.

- Users may download and print one copy of any publication from the public portal for the purpose of private study or research.
- You may not further distribute the material or use it for any profit-making activity or commercial gain
- You may freely distribute the URL identifying the publication in the public portal

If you believe that this document breaches copyright please contact us providing details, and we will remove access to the work immediately and investigate your claim.

Research article

Satoshi Ishii*, Makoto Higashino, Shinya Goya, Evgeniy Shkondin, Katsuhisa Tanaka, Tadaaki Nagao, Osamu Takayama and Shunsuke Murai

Extreme thermal anisotropy in high-aspect-ratio titanium nitride nanostructures for efficient photothermal heating

<https://doi.org/10.1515/nanoph-2020-0569>

Received October 12, 2020; accepted December 21, 2020;

published online February 26, 2021

Abstract: High optical absorptivity or a large absorption cross-section is necessary to fully utilize the irradiation of light for photothermal heating. Recently, titanium nitride (TiN) nanostructures have been demonstrated to be robust optical absorbers in the optical range owing to their non-radiative decay processes enhanced by broad plasmon resonances. Because the photothermally generated heat dissipates to the surroundings, suppressing heat transfer from TiN nanostructures is crucial for maximizing the photothermal temperature increase. In the current work, compared to the planar TiN film, high-aspect-ratio TiN nanostructures with subwavelength periodicities have been demonstrated to enhance the photothermal

temperature increase by a 100-fold using nanotube samples. The reason is attributed to the extremely anisotropic effective thermal conductivities. Our work has revealed that high-aspect-ratio TiN nanostructures are effective in improving photothermal heating, and they can be used in various applications, such as solar heating, chemical reactions, and microfluidics.

Keywords: effective medium theory; nanostructure; photothermal effect; surface plasmon; transition metal nitride.

1 Introduction

Photothermal heating occurs when an optically irradiated material absorbs incident light. Although metals are reflective in general, metallic nanostructures typically exhibit higher optical absorption compared to that of bulk form or thin films owing to reduced reflectivities or increased absorption cross sections, which results in local heating. When metallic nanostructures excite plasmon resonances, optical absorptions are further enhanced [1, 2]. In plasmonic photothermal heating, the heated region can be confined even to the subwavelength scale. This unique feature renders these nanostructures suitable for various applications such as photothermal imaging [3, 4], optical trapping [5, 6], optofluidics [7–9], material growth [10], and chemical reactions [11].

When we consider materials for plasmonic photothermal heating, gold has been exclusively used owing to its well-known plasmonic properties and chemical stability [12–14]. However, recent studies have shown that despite being a ceramic, titanium nitride, which is of transition metal nitrides, can be an alternative material for plasmonic photothermal heating. It should be noted that although the radiative plasmonic properties of TiN are inferior to those of gold, TiN is superior to gold in terms of photothermal heating. This is because the optical losses in TiN are moderately larger than those in gold so that the absorption

*Corresponding author: **Satoshi Ishii**, International Center for Materials Nanoarchitectonics (MANA), National Institute for Materials Science (NIMS), 1-1 Namiki, Tsukuba, Ibaraki, 305-0044, Japan; Faculty of Pure and Applied Physics, University of Tsukuba, Tsukuba, Ibaraki, 305-8577, Japan; and PRESTO, Japan Science and Technology Agency, Saitama, 332-0012, Japan, E-mail: sishii@nims.go.jp. <https://orcid.org/0000-0003-0731-8428>

Makoto Higashino, Shinya Goya, Katsuhisa Tanaka and Shunsuke Murai, Department of Material Chemistry, Graduate School of Engineering, Kyoto University, Katsura, Nishikyo-ku, Kyoto, 615-8510, Japan, E-mail: murai.shunsuke.2m@kyoto-u.ac.jp (S. Murai). <https://orcid.org/0000-0002-4597-973X> (S. Murai)

Evgeniy Shkondin, DTU Nanolab—National Center for Micro- and Nanofabrication, Technical University of Denmark, Kgs. Lyngby, 2800, Denmark. <https://orcid.org/0000-0002-8347-1814>

Tadaaki Nagao, International Center for Materials Nanoarchitectonics (MANA), National Institute for Materials Science (NIMS), 1-1 Namiki, Tsukuba, Ibaraki, 305-0044, Japan; and Department of Condensed Matter Physics, Graduate School of Science, Hokkaido University, Sapporo, Hokkaido, 060-0810, Japan. <https://orcid.org/0000-0002-6746-2686>

Osamu Takayama, DTU Fotonik—Department of Photonics Engineering, Technical University of Denmark, Kgs. Lyngby, 2800, Denmark, E-mail: otak@fotonik.dtu.dk. <https://orcid.org/0000-0003-3525-3262>

is enhanced by plasmon resonances. Nevertheless, precautions are necessary as considerably large losses diminish plasmon resonances, leading to an insignificant enhancement [15]. Another advantage of TiN over metals is that since TiN exhibits characteristic Raman spectrum due to the defects [16, 17], its Raman spectrum can be used as a thermometer [18, 19], which enables us to monitor the temperature during photothermal heating. Active research on plasmonic photothermal heating with TiN has been carried out during the past decade, and it includes local heating by nanodisks [20], solar heating including solar distillation [21–23], cancer therapy [24], and chemical reactions [25].

Because an efficient photothermal heating process maximizes the temperature increase at a fixed optical power, increasing the optical absorptivity or absorption cross section is a prerequisite. An equally critical condition is to suppress heat dissipation from the optically irradiated area. In a situation where plasmonic nanostructures are fixed on a substrate, and the superstrate is air, the major source of heat dissipation is the heat conduction to the substrate. Therefore, a simple method to suppress heat conduction is to use a low thermal conductive substrate or a membrane [19]. However, the choice of substrate often has restrictions, and the membrane may not be suitable for applications in harsh conditions or large areas.

The substrate dependence can be eliminated if a plasmonic photothermal nanostructure with a high optical absorptivity and low thermal conductance is used. Fabricating high-aspect-ratio samples, which can be considered as a porous structure (or sparse structure), fits this requirement. The anisotropic nature of the effective thermal conductivities of these structures have been studied analytically [26], and experimental works have been performed on structures such as porous alumina [27, 28] and porous silicon [29]. Thus far, each component of an anisotropic thermal conductivity has been measured by component by component using various techniques [27–29]. However, the heat conduction from a point heat source, which is the case with heating by a focused laser beam, involves heat conduction along three dimensions such that all three components affect heat conduction inside the anisotropic medium. When engineering the effective thermal conductivity of nanostructures, the geometries play a major role in reducing the heat conduction. Most of the structures that have been studied so far were hole arrays which were connected in lateral directions. In contrast, trench and pillar (including tube) arrays are disconnected in lateral directions, which are considered to be effective in lowering the effective thermal conductivities.

In the current work, we fabricated high-aspect-ratio TiN tubes and TiN trench structures with subwavelength periodicities and investigated the photothermal heating properties by Raman spectroscopy. Compared to the planar TiN film, the photothermal surface temperature increased by more than 100-fold, where the tube showed the highest enhancement. According to the finite element heat transfer analyses, enhanced photothermal heating originated from the extremely anisotropic effective thermal conductivities. The high-aspect-ratio nanostructures caused increased optical absorptivities and a lowered thermal conductance, which can potentially improve photothermal heating applications drastically.

2 Results and discussion

For sample fabrication, we basically followed a procedure that was developed earlier [30–32]. Briefly, for the tube sample, a Si mold was fabricated by deep UV (DUV) lithography and deep reactive ion etching (DRIE), where the BOSCH process was used in the DRIE to etch approximately 2.4 μm . Then, approximately 90-nm thick TiN layers were formed on the Si mold by the atomic layer deposition (ALD) technique. In the final step, excess TiN and Si were etched to obtain the desired structure. The fabrication procedure for the trench sample was similar. A 150-nm thick TiN film was fabricated on a Si wafer by the ALD technique under the similar conditions used to fabricate the tube. The details can be found in the Methods and Supporting Information Figure S1.

Figure 1(a) and (b) presents the schematic and tilted-view SEM images of the tube and trench samples on the Si wafers, respectively. The periods are 400 nm for both samples, and heights are 2.36 and 2.26 μm for the tube and trench, respectively. For the tube sample, the inner and outer diameters of the tube are 89 and 265 nm, respectively. For the trench sample, the trench width is 200 nm. Thus, the tube and trench samples have aspect ratios of approximately 8.9 and 11, respectively.

Figure 2(a) and (b), respectively, displays the measured and numerically calculated reflectance (R) of the samples upon illumination with linearly polarized light. Because the trench has polarization dependence, the reflectance of the trench sample was measured in perpendicular and parallel directions, where the polarizations were perpendicular and parallel to the trench, respectively. The numerical calculations were based on the finite element method, where the experimentally obtained complex permittivity of TiN [30] was used as the optical constant of TiN, and the geometrical parameters were

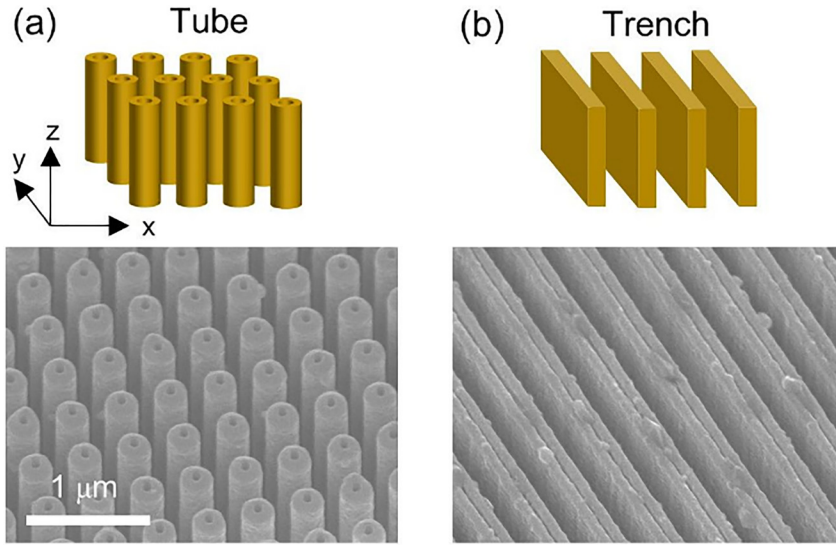


Figure 1: Schematics and SEM images of (a) TiN tube and (b) TiN trench on Si substrates. The SEM images were taken at 30° tilt.

acquired from the SEM images. Evidently, the experimental and numerical results are in reasonable agreements. Possible reasons for the discrepancies between the experimental and numerical results are minor errors in obtaining the TiN permittivity from the spectroscopic measurements and imperfection in the sample geometries. Overall, the order of the reflectance in the visible region from the lowest to the highest is tube, trench (\perp), trench (\parallel), and film. As all four samples did not exhibit transmittance in the visible because of the Si substrates, the absorptance was calculated as $(100\% - R)$. The calculated absorptance of the tube, trench (\perp), trench (\parallel), and film are 91, 81, 47, and 35 %, respectively, where the measured reflectance was used.

To understand the differences in the optical properties, the field map of each structure is analyzed as follows (Figure 2(c)). The relatively high reflectance of the film was due to the negative permittivity of TiN [30]. For the tube sample, the tube array, which had subwavelength periodicity and high aspect ratio, performed as an antireflection structure. For the trench sample, by considering the TiN and air as metal and insulator, respectively, the trench acted as a periodically ordered 1D metal–insulator–metal (MIM) waveguide. Further, perpendicularly polarized incident light to the trench can be regarded as TM-polarized wave propagations in MIM waveguides. Because a TM-polarized wave propagation in an MIM

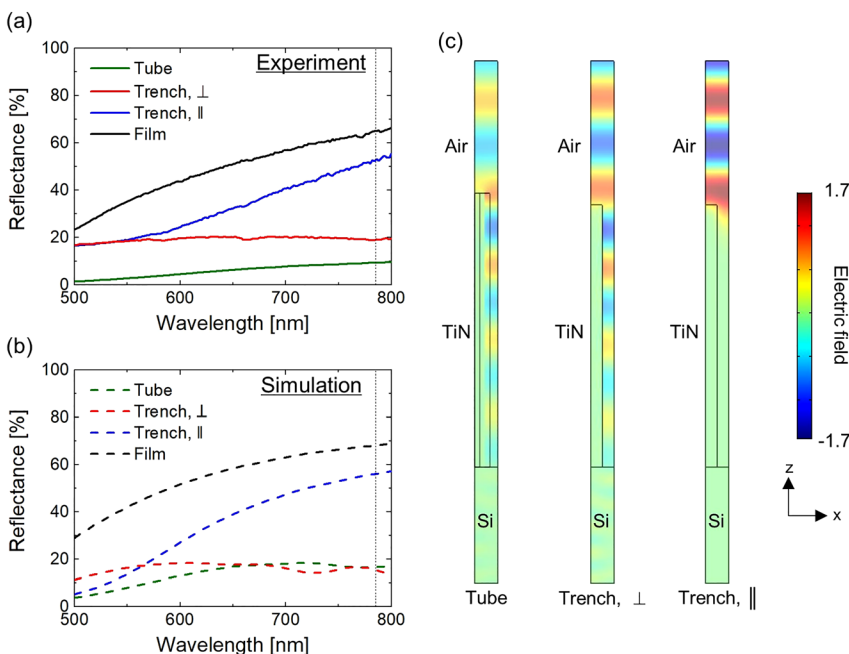


Figure 2: Reflectance of the samples from (a) UV–VIS measurements and (b) numerical simulations. The dashed line in each figure marks 785 nm in the wavelength scale. In the simulations, the incident fields were linearly polarized. (c) The cross-sectional electric field maps in the x – z plane by irradiating linearly polarized light at 785 nm for the tube, trench (\perp), and trench (\parallel). One half of each period is shown. The color scale is common for the three field maps and is normalized to the incident field.

waveguide does not have a cutoff, incident light can propagate deep inside the trench to get absorbed even though free-space wavelengths are longer than the period. In contrast, parallel polarized incident light to the trench can be assumed similar to the TE-polarized wave propagations in MIM waveguides, and they have a cutoff. Thus, parallel polarized light is mainly reflected without propagating inside the trench.

To evaluate the effective thermal conductivity of the samples, the samples were photothermally heated by a CW laser with a wavelength of 785 nm. The sample surface temperatures at the laser irradiation were evaluated from the temperature-dependent Stokes peak shift at 785 nm excitation [19]. Basically, the 785-nm laser was used not only to heat the samples but also for Raman spectroscopy. Because the optical property of TiN largely depends on the fabrication conditions, the temperature-dependent Stokes peak at $\sim 565 \text{ cm}^{-1}$ [18] was measured for the current film sample, and the relationship shown in Figure S2 was used to estimate the sample surface temperature. Except for the tube sample, the Stokes peak shifted to smaller wavenumbers with respect to the incident laser power, indicating an increase in temperature. The Stokes peak of the tube sample shifted to a larger wavenumber with respect to the incident laser power. This opposite trend was likely caused by the damage that was already visible at 2 mW. The origin of the damage was the oxidation of TiN, which typically occurs at approximately 800 K under ambient condition [33, 34]. The damage appeared at 7 and 10 mW for trench (\perp) and trench (\parallel), respectively, whereas the film sample was not damaged even at 40 mW, which was the maximum laser power. Images of the damages are presented in Figure 3(a). From the damage threshold, the following order for the surface temperature increase is estimated: tube > trench (\perp) > trench (\parallel) > film. Although the height of the tube and trench were only 2.26 and 2.36 μm , respectively, which were more than two orders of magnitude smaller than the corresponding substrate thicknesses, the nanostructures had significant effects on the temperature increase owing to photothermal heating.

The incident laser power dependences of the sample surface temperatures extracted from the Raman spectra are illustrated in Figure 3(b). As seen from Figure 3(b), while the laser power which created damage was expected to reach above $\sim 800 \text{ K}$, the extracted temperature is far lower than $\sim 800 \text{ K}$. This is due to the appearance of titanium oxide peak [35] and decrease of TiN phase reduced the $\sim 565 \text{ cm}^{-1}$ peak which was used to extract temperature. Thus, the dashed lines were guide to the eye which follow the trend of the filled marks indicating no damage. The temperature increase was the highest for the tube sample

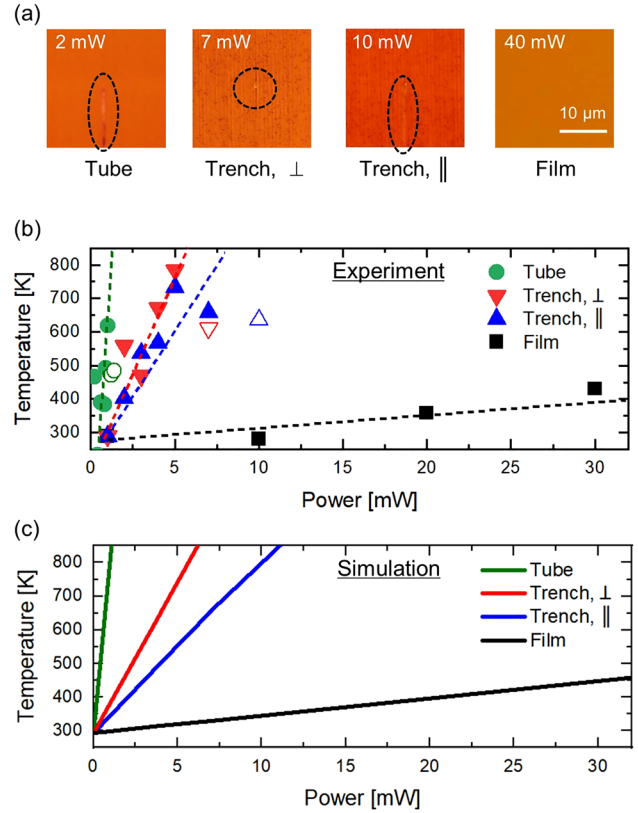


Figure 3: (a) Optical microscope images of the four samples. For tube, trench (\perp), and trench (\parallel), the damages are visible when the incident laser powers after the objective lens were 2, 7, and 10 mW, respectively. For film, there was no damage even at 40 mW. Power-dependent surface temperature (b) extracted from Raman spectroscopy measurements and (c) numerical simulations based on finite element method. In panel (b), filled mark (unfilled mark) indicates that the irradiated position was not damaged (damaged) at the laser power. The dashed lines, which exclude the unfilled marks, are for the convenience to follow the trend. The reason for excluding the unfilled marks is that the extracted temperatures with damages underestimate the temperatures.

and decreased in the following order: trench (\perp), trench (\parallel), and film. Note that the differences in the temperature increase between the samples are larger than the differences in the absorbance, indicating the pivotal role of the nanostructured parts in modulating the effective thermal conductivities.

To evaluate the effective thermal conductivities of the nanostructured parts, the thermal conductance was modeled for each unit cell by applying temperature differences in the x , y , and z directions, and solved using the finite element method [36]. Both tube and trench resulted in uniaxial thermal conductivities; [0.05, 0.05, 8.4] and [0.05, 15, 15] in W/m/K for the tube and trench, respectively. The differences in the ordinary and extraordinary components of the tube and trench are more than two

orders of magnitude. Such extreme uniaxial thermal conductivities stemmed from the significantly different thermal conductivity magnitudes of TiN (28.84 W/m/K) [37] and air (0.026 W/m/K). Using these effective thermal conductivities for the nanostructured parts, heat transfer analyses that modeled the experimental conditions were carried out using the finite element method. The simulated surface temperature against the incident laser power is shown in Figure 3(c). The simulations qualitatively agree with the experimental results, although the simulated temperature for trench (||) is overestimated compared with the corresponding experimental result. Overall, we conclude that the enhanced photothermal heating observed for the nanostructured samples originated from the extreme anisotropy of the thermal conductivities realized by the high-aspect-ratio nanostructures.

From the simulated values, compared with the film, the photothermal temperature increase was enhanced by approximately 10-fold even for the trench (||). For the trench (\perp) and tube, the corresponding enhancements were approximately 17-fold and 101-fold, respectively.

The anisotropic nature of the effective thermal conductivities can be verified through both experiments and simulations. In the experiments, laser damage was created on the trench at parallel and perpendicular polarizations by a 20x objective lens (NA0.25, SLMPlam N, Olympus) and was observed by a 50x objective lens (NA0.80, MPlan FLM, Olympus), which has a better resolution. The resultant damage is displayed in Figures 4(a) and S3. Regardless of the polarization, the damage shapes are elliptical with the long axes parallel to the trench. The simulated surface temperature profiles by irradiating a Gaussian beam also exhibit elliptical profiles along the trench direction. Because the effective thermal conductivity parallel to the trench is more than two orders of magnitude larger than that perpendicular to the trench, heat dissipation in the perpendicular direction was suppressed, resulting in the elliptical damage and elliptical temperature profiles. In contrast, for the tube sample, a circular damage spot and circular temperature profile can be seen in Figure S4. This is because the effective thermal conductivity components in the x and y directions are identical.

Our studies have demonstrated that high-aspect-ratio nanostructures with heights of only a few micrometers can significantly increase photothermal heating. To evaluate the impact of thickness on the surface temperature of the laser-irradiated area, numerical heat transfer simulations were performed for the tube structure, as shown in Figure S5. In the simulations, the effective thermal conductivity of the tube was used, which was similar to the above simulations. The results show a considerably higher

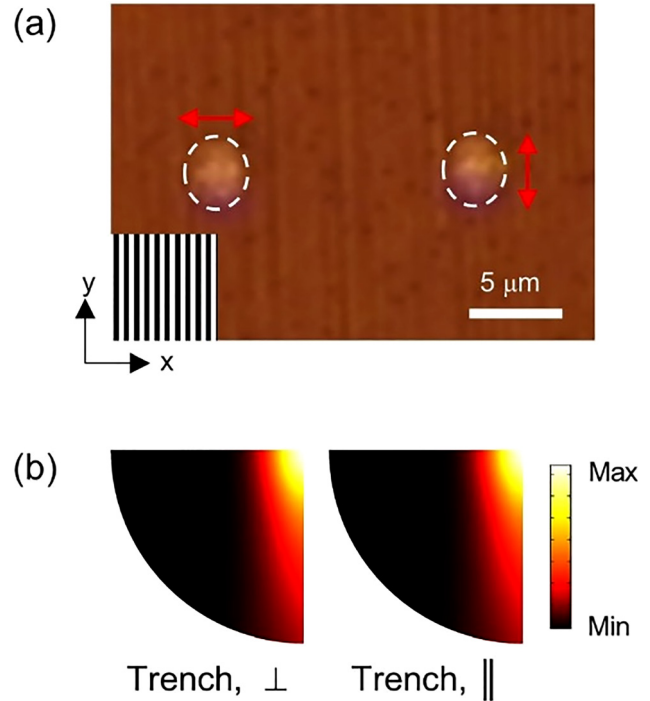


Figure 4: (a) Optical microscope image of the trench after creating damages with the 785 nm laser at perpendicular and parallel polarizations. The trench direction was aligned to the x -axis. The boundaries of the damages are marked by white dashed lines. The inset shows the direction of the trench, and red arrows show the polarization directions. (b) Numerically simulated surface temperature profiles for trench (\perp) and trench (||) showing one-fourth of the heated areas. In the simulations, the nanostructured layers were modeled as effective media, as described in the main text. Each color map is normalized by its maximum value, and the minimum temperatures are 293 K for both maps. The radii of the color maps are 2 μm .

photothermal heating with increasing tube height; however, the heating efficiency starts to saturate above a tube height of ~ 20 μm . This is because the majority of the heat dissipation takes place within ~ 20 μm from the surface. In reality, fabrication becomes significantly challenging if the aspect ratio exceeds 10.

During the past decade, different types of plasmonic nanostructures have been developed to enhance the optical absorption and generate heat at the nanoscale. However, because their heights are a few tens of nanometers, the heat generated at the nanostructures dissipates into the substrates before high temperatures are realized in the irradiated area. Our study has verified that a subwavelength high-aspect-ratio structure not only exhibits high optical absorptivity but also significantly reduces thermal conductivity, which, in turn, enhances photothermal heating. Although not all three anisotropic thermal conductivity components have low values, realization

of at least one low-value component (e.g., extraordinary component of the trench) notably improved photothermal heating. Nevertheless, the tube sample has superior photothermal properties because two out of the three components of the anisotropic thermal conductivity are significantly low. Further, these unique properties of the high-aspect-ratio TiN nanostructures are expected to enable them to drastically improve existing applications such as solar water distillation [23] and chemical reactions [25]. Moreover, in high-temperature applications under ambient conditions, oxidation of TiN to titanium oxide is a problem because titanium oxide is not a metal and does not show plasmonic effect. This drawback of TiN can be overcome by overcoating TiN by silicon nitride [38] or alumina [34] that was found to be effective in increasing the threshold temperature of TiN oxidation [34].

Adopting a high-aspect-ratio nanostructure to realize low thermal conductivity is expected to work for other materials. Using low thermal conductivity materials such as silica or zirconia for nanostructures should result in even lower thermal conductivity than the current samples. However, certain precautions need to be exercised before using these materials for photothermal heating in the visible and near infrared range. As these materials are transparent, a coating of a thin absorbing layer is necessary for visible and near-infrared absorption.

3 Conclusion

To summarize, we have experimentally and numerically demonstrated that the high-aspect-ratio TiN tube and trench nanostructures exhibit significantly higher photothermal heating effects than the TiN film. This is attributed to their high optical absorptances owing to the plasmonic losses in TiN and, more importantly, to their significantly reduced anisotropic effective thermal conductivities. For the tube, the enhancement factor was as high as 101. Among the tubes and trenches, the tube had higher photothermal properties because two out of the three components of the anisotropic thermal conductivity have three orders of magnitude smaller than the bulk thermal conductivity of TiN. Even height of a few micrometers of those structures were sufficient to suppress the heat conduction to the substrates and subsequently enhance the photothermal heating by the incident laser. High-aspect-ratio nanostructures in the current work have potential applications in chemical reactions and liquid evaporation, including solar water desalination, where high temperatures are required.

4 Experimental section

4.1 Sample fabrication

TiN thin films were deposited by ALD technique in a commercial hot-wall reactor (R-200 Advanced Plasma ALD, Picosun) at 500 °C. The sequential introduction of TiCl_4 and NH_3 precursors ensured linear growth with a deposition rate of 0.027 nm/cycle. The films were deposited with 3300 and 5300 cycles, which correspond to thicknesses of approximately 90 and 150 nm, respectively. The prepared samples were annealed in a conventional annealing furnace (PEO-604, ATV technology) at 900 °C. The process was performed in a vacuum with 2 sccm flow of N_2 for 1 h. Prior to processing, the chamber was flushed with nitrogen for 1 h to ensure the absence of environmental oxygen, which could cause undesirable oxidation during the annealing. The heating from room temperature to the desired process temperature was performed at a rate of 30 °C/min, and the final cooling took 2.5 h.

TiN tube with a height, pitch, diameter, and wall thickness of 2360, 400, 265, and 88 nm, respectively, was fabricated by the combination of DUV lithography, DRIE, and ALD techniques, as depicted in Figure S1. First, the photoresist template was prepared on a 600-nm thick Si wafer by spin-coating 65 nm BARC (DUV42S-6) and 360 nm positive tone DUV resist (KRF 230Y) using a spin-coating system (Gamma 2 M spin-coater, Süss MicroTech). Final patterns were defined by a DUV stepper (FPA-3000EX4, Canon) exposure and subsequent development in tetramethylammoniumhydroxid (TMAH) solution. The subsequent steps in fabrication were BARC etching in oxygen plasma, preparation of deep holes in silicon by the implementation of the BOSCH process, and remaining photoresist stripping. All three steps were performed in the same etching system (DRIE Pegasus, SPTS). The prepared silicon templates were passivated with approximately 90 nm TiN in a hot-wall ALD reactor at 500 °C using TiCl_4 and NH_3 precursors. After deposition, the structures were annealed for 1 h at 900 °C in an annealing furnace. The final procedure included the removal of the top part of the TiN coating and etching of the silicon template to obtain the final product, high-aspect-ratio TiN tubes attached to the silicon platform. This final step was completed using the same ICP tool (PRO ICP from SPTS) using Cl_2 -based plasma and SF_6 for etching of TiN and silicon, respectively.

Similarly, a TiN trench with a height, pitch, and width of 2260, 400, and 200 nm, respectively, was also fabricated by a similar process.

4.2 Optical characterization

The reflectance was measured with a UV-VIS spectrometer (SolidSpec-3700, Shimadzu). Raman spectroscopy was carried out with a micro Raman system (Alpha 300S, WITec) equipped with a 785 nm CW laser, which was used to heat the samples and excite Raman scattering. Raman spectroscopy was performed using a 50x objective lens (NA0.80, MPlan FLM, Olympus). To obtain the temperature-dependent Stokes peak relationship, a sample heater (10064, Japan High Tech) was used to heat the sample. To create and observe laser damage, a microscope of the micro Raman system was used.

4.3 Numerical calculations

Electromagnetic simulations were performed using commercial software based on the finite element method (COMSOL Multiphysics). The geometrical parameters were obtained from the SEM images. The permittivities of TiN and Si were acquired from the studies by Shkondin et al. [30, 39], respectively.

Heat transfer simulations were also performed using COMSOL Multiphysics. To simulate the effective thermal conductivities, the actual geometrical parameters of the nanostructure unit cells were used, and the temperature differences were applied in the x , y , and z directions. To simulate the surface temperatures, the incident beam was modeled as an incoming heat flux with a Gaussian profile, and the nanostructures were homogenized as effective layers having identical thicknesses as the actual nanostructures. The heat transfer modeling included convective heat transfer and radiative heat transfer from the surfaces.

Acknowledgments: The authors would like to thank Min-Wen Yu and Nicholas Tanjaya for their help in optical characterization, and acknowledge the support from the National Centre for Nano Fabrication and Characterization (DTU Nanolab) for the fabrication of samples.

Author contributions: S.I., S.M., and O.T. conceived the idea of the experiments. E.S. fabricated the samples, and S.G. and M.H. characterized the samples. All authors were involved in the discussion and manuscript writing.

Research funding: S.I. acknowledges the support from PRESTO “Thermal Science and Control of Spectral Energy Transport” (JPMJPR19I2), Kakenhi from JSPS, Japan (17H04801), the TEPCO Memorial Foundation, and the Japan Association for Chemical Innovation. O.T.’s contribution was supported by the Independent Research Fund Denmark, DFF Research Project 2 “PhotoHub” (8022-00387B).

Conflict of interest statement: The authors declare no competing interests.

References

- [1] G. Baffou and R. Quidant, “Thermo-plasmonics: using metallic nanostructures as nano-sources of heat,” *Laser Photonics Rev.*, vol. 7, pp. 171–187, 2013.
- [2] M. L. Brongersma, N. J. Halas, and P. Nordlander, “Plasmon-induced hot carrier science and technology,” *Nat. Nanotechnol.*, vol. 10, pp. 25–34, 2015.
- [3] D. Boyer, P. Tamarat, A. Maali, B. Lounis, and M. Orrit, “Photothermal imaging of nanometer-sized metal particles among scatterers,” *Science*, vol. 297, pp. 1160–1163, 2002.
- [4] G. Baffou, C. Girard, and R. Quidant, “Mapping heat origin in plasmonic structures,” *Phys. Rev. Lett.*, vol. 104, p. 136805, 2010.
- [5] J. C. Ndukaife, A. V. Kildishev, A. G. A. Nnanna, V. M. Shalaev, S. T. Wereley, and A. Boltasseva, “Long-range and rapid transport of individual nano-objects by a hybrid electrothermoplasmonic nanotweezer,” *Nat. Nanotechnol.*, vol. 11, pp. 53–59, 2016.
- [6] T. Shoji, K. Itoh, J. Saitoh, et al., “Plasmonic manipulation of DNA using a combination of optical and thermophoretic forces: separation of different-sized DNA from mixture solution,” *Sci. Rep.*, vol. 10, p. 3349, 2020.
- [7] G. L. Liu, J. Kim, Y. Lu, and L. P. Lee, “Optofluidic control using photothermal nanoparticles,” *Nat. Mater.*, vol. 5, pp. 27–32, 2006.
- [8] J. S. Donner, G. Baffou, D. McCloskey, and R. Quidant, “Plasmon-assisted optofluidics,” *ACS Nano*, vol. 5, pp. 5457–5462, 2011.
- [9] K. Namura, K. Nakajima, and M. Suzuki, “Quasi-stokeslet induced by thermoplasmonic Marangoni effect around a water vapor microbubble,” *Sci. Rep.*, vol. 7, p. 45776, 2017.
- [10] L. Cao, D. N. Barsic, A. R. Guichard, and M. L. Brongersma, “Plasmon-assisted local temperature control to pattern individual semiconductor nanowires and carbon nanotubes,” *Nano Lett.*, vol. 7, pp. 3523–3527, 2007.
- [11] D. A. Boyd, L. Greengard, M. Brongersma, M. Y. El-Naggar, and D. G. Goodwin, “Plasmon-assisted chemical vapor deposition,” *Nano Lett.*, vol. 6, pp. 2592–2597, 2006.
- [12] K. Namura, M. Suzuki, K. Nakajima, and K. Kimura, “Heat-generating property of a local plasmon resonator under illumination,” *Opt. Lett.*, vol. 36, pp. 3533–3535, 2011.
- [13] N. J. Hogan, A. S. Urban, C. Ayala-Orozco, A. Pimpinelli, P. Nordlander, and N. J. Halas, “Nanoparticles heat through light localization,” *Nano Lett.*, vol. 14, pp. 4640–4645, 2014.
- [14] A. R. Rastinehad, H. Anastos, E. Wajswol, et al., “Gold nanoshell-localized photothermal ablation of prostate tumors in a clinical pilot device study,” *Proc. Natl. Acad. Sci.*, vol. 116, pp. 18590–18596, 2019.
- [15] S. Ishii, S. L. Shinde, and T. Nagao, “Nonmetallic materials for plasmonic hot carrier excitation,” *Adv. Opt. Mater.*, vol. 7, p. 1800603, 2019.
- [16] W. Spengler and R. Kaiser, “First and second order Raman scattering in transition metal compounds,” *Solid State Commun.*, vol. 18, pp. 881–884, 1976.
- [17] W. Spengler, R. Kaiser, A. N. Christensen, and G. Müller-Vogt, “Raman scattering, superconductivity, and phonon density of states of stoichiometric and nonstoichiometric TiN,” *Phys. Rev. B*, vol. 17, pp. 1095–1101, 1978.
- [18] I. Dreiling, A. Haug, H. Holzschuh, and T. Chassé, “Raman spectroscopy as a tool to study cubic Ti–C–N CVD coatings,” *Surf. Coating. Technol.*, vol. 204, pp. 1008–1012, 2009.
- [19] S. Ishii, R. Kamakura, H. Sakamoto, et al., “Demonstration of temperature-plateau superheated liquid by photothermal conversion of plasmonic titanium nitride nanostructures,” *Nanoscale*, vol. 10, pp. 18451–18456, 2018.
- [20] U. Guler, J. C. Ndukaife, G. V. Naik, et al., “Local heating with lithographically fabricated plasmonic titanium nitride nanoparticles,” *Nano Lett.*, vol. 13, pp. 6078–6083, 2013.
- [21] S. Ishii, R. P. Sugavaneshwar, and T. Nagao, “Titanium nitride nanoparticles as plasmonic solar heat transducers,” *J. Phys. Chem. C*, vol. 120, pp. 2343–2348, 2016.

- [22] S. Ishii, K. Uto, E. Niiyama, M. Ebara, and T. Nagao, "Hybridizing poly (ϵ -caprolactone) and plasmonic titanium nitride nanoparticles for broadband photoresponsive shape memory films," *ACS Appl. Mater. Interfaces*, vol. 8, pp. 5634–5640, 2016.
- [23] M. Kaur, S. Ishii, S. L. Shinde, and T. Nagao, "All-ceramic solar-driven water purifier based on anodized aluminum oxide and plasmonic titanium nitride," *Adv. Sustain. Syst.*, vol. 3, p. 1800112, 2019.
- [24] W. He, K. Ai, C. Jiang, Y. Li, X. Song, and L. Lu, "Plasmonic titanium nitride nanoparticles for in vivo photoacoustic tomography imaging and photothermal cancer therapy," *Biomaterials*, vol. 132, pp. 37–47, 2017.
- [25] A. Naldoni, Z. A. Kudyshev, L. Mascaretti, et al., "Solar thermoplasmonic nanofurnace for high-temperature heterogeneous catalysis," *Nano Lett.*, vol. 20, pp. 3663–3672, 2020.
- [26] D. P. H. Hasselman and L. F. Johnson, "Effective thermal conductivity of composites with interfacial thermal barrier resistance," *J. Compos. Mater.*, vol. 21, pp. 508–515, 1987.
- [27] D.-A. Borca-Tasciuc and G. Chen, "Anisotropic thermal properties of nanochanneled alumina templates," *J. Appl. Phys.*, vol. 97, p. 084303, 2005.
- [28] B. Abad, J. Maiz, A. Ruiz-Clavijo, O. Caballero-Calero, and M. Martin-Gonzalez, "Tailoring thermal conductivity via three-dimensional porous alumina," *Sci. Rep.*, vol. 6, p. 38595, 2016.
- [29] D. Song and G. Chen, "Thermal conductivity of periodic microporous silicon films," *Appl. Phys. Lett.*, vol. 84, pp. 687–689, 2004.
- [30] E. Shkondin, T. Repän, O. Takayama, and A. V. Lavrinenko, "High aspect ratio titanium nitride trench structures as plasmonic biosensor," *Opt. Mater. Express*, vol. 7, pp. 4171–4182, 2017.
- [31] E. Shkondin, T. Repän, M. E. Aryaee Panah, A. V. Lavrinenko, and O. Takayama, "High aspect ratio plasmonic nanotrench structures with large active surface area for label-free mid-infrared molecular absorption sensing," *ACS Appl. Nano Mater.*, vol. 1, pp. 1212–1218, 2018.
- [32] E. Shkondin, H. Alimadadi, O. Takayama, F. Jensen, and A. V. Lavrinenko, "Fabrication of hollow coaxial $\text{Al}_2\text{O}_3/\text{ZnAl}_2\text{O}_4$ high aspect ratio freestanding nanotubes based on the Kirkendall effect," *J. Vac. Sci. Technol. A*, vol. 38, p. 013402, 2020.
- [33] M. P. Wells, R. Bower, R. Kilmurray, et al., "Temperature stability of thin film refractory plasmonic materials," *Opt. Express*, vol. 26, pp. 15726–15744, 2018.
- [34] S. Goya, S. Murai, and K. Tanaka, "Thermal oxidation of TiN nanocylinder arrays: effects of insulator coatings by atomic layer deposition," *Opt. Mater. Express*, vol. 9, pp. 4751–4764, 2019.
- [35] F. Hardcastle, "Raman spectroscopy of titania (TiO_2) nanotubular water-splitting catalysts," *J. Ark. Acad. Sci.*, vol. 65, pp. 43–48, 2011.
- [36] P. Berne, "Thermal conductivity of composites: how COMSOL revealed an omission in a classical paper," in *2015 COMSOL Conference*, Grenoble, COMSOL, 2015.
- [37] J. F. Shackelford, Y.-H. Han, S. Kim, and S.-H. Kwon, *CRC Materials Science and Engineering Handbook*, CRC Press, 2016.
- [38] U. G. Jingjing Liu, A. Lagutchev, A. Kildishev, O. Malis, A. Boltasseva, V. Shalaev, "Quasi-coherent thermal emitter based on refractory plasmonic materials," *Opt. Mater. Express*, vol. 5, pp. 2721–2728, 2015.
- [39] E. D. Palik, *Handbook of Optical Constants of Solids*, Academic Press, 1985.

Supplementary Material: The online version of this article offers supplementary material (<https://doi.org/10.1515/nanoph-2020-0569>).